JMEPEG
https://doi.org/10.1007/s11665-023-07810-y

TECHNICAL ARTICLE

Ce Effects on Dynamic Recrystallization of Cu-Fe-Ti-Mg Alloys Due to Hot Compression

Qingbao Cao, Meng Zhou, Yi Zhang, Haoyan Hu, Xu Li, Baohong Tian, Yanlin Jia, Yong Liu, and Alex A. Volinsky

Submitted: 19 September 2022 / Revised: 20 November 2022 / Accepted: 20 December 2022

This study researched how Ce addition affects the microstructure and mechanical behavior of Cu-Fe-Ti-Mg alloys during hot compression. A thermal deformation simulation machine was used to study the hot compression process at 0.001-10 s^{-1} strain rates and 500-950 °C deformation temperatures. The true stress–strain curves and constitutive equations were obtained for the two alloys. Based on the electron backscatter diffraction analysis, the addition of Ce can improve the dislocation density and texture strength of the Cu-Fe-Ti-Mg alloy. The microstructure and precipitates of the Cu-Fe-Ti-Mg-Ce alloy were also analyzed. The average grain size of the Cu-Fe-Ti-Mg-Ce alloy is smaller than the Cu-Fe-Ti-Mg alloy. The addition of Ce delayed dynamic recrystallization. These findings provide a theoretical foundation for understanding the Ce addition effects on the hot deformation behavior of the Cu-Fe-Ti-Mg alloy, serving as a reference for industrial manufacturing of the alloy.

Keywords constitutive equations, Cu-Fe-Ti-Mg and Cu-Fe-Ti-Mg-Ce alloys, hot compression, microstructure, texture strength

1. Introduction

Due to their high strength, electrical conductivity, corrosion resistance, and thermal conductivity, copper alloys are commonly used in aircraft, marine applications, and lead frames (Ref 1-5). With the miniaturization of electronic devices, the performance of copper alloys needs to be improved. For example, the power consumption of the lead frame of an integrated circuit increases exponentially with decreasing size, requiring not only great heat dissipation but also good tensile strength and overall mechanical properties. At present, the common way to improve the mechanical properties of copper-based materials is to add alloying elements, such as iron, phosphorus, magnesium, chromium, and zinc. The addition of Fe to Cu can refine the grain, while the addition of Ti can improve the strength and wear resistance of the alloy, and the addition of a certain amount of Mg can improve the electrical conductivity of the alloy. For example, Cu-Fe-P and Cu-Cr-Zr alloys are used for lead frames (Ref 6, 7), while Cu-Mg and Cu-Sn alloys are used for railway contact wires (Ref 8, 9). Therefore, according to the phase diagrams, Cu-0.7Fe-0.35Ti-0.08Mg and Cu-0.7Fe-0.35Ti-0.08Mg-0.15Ce alloys were designed. It is expected that the Fe_2Ti phase can be precipitated to obtain high performance.

Shi et al. (Ref 10) prepared the Cu-Fe alloy and found fine dispersed iron nanoparticles coherent with the copper matrix. Lu et al. (Ref 11) found that the addition of trace amounts of B and Ce greatly increased the recrystallization temperature of the Cu-Fe-P alloy, resulting in excellent overall properties. Wang et al. (Ref 12) studied the effects of Ce and Y elements on the microstructure and secondary phases precipitation in the Cu-Mg-Fe alloy during hot compression and found that adding Ce could significantly improve the flow stress and activation energy of the alloy, and delay the dynamic recrystallization (DRX). Li et al. (Ref 13) found that strain hardening, recovery, and fine grain strengthening at different temperatures improved the plastic deformation behavior of the Cu-8.0Ni-1.8Si-0.15Mg alloy. Zhang et al. (Ref 14) found that the presence of iron-rich particles nails dislocations, thus increasing the activation energy and flow stress of the Cu-Fe-P alloy, refining recrystallized grains. Zhao et al. (Ref 15) studied Cu-15Ni-8Sn alloys and added Ti and Si, resulting in better strength and ductility. Ban et al. (Ref 16) found that adding Cr to Cu-Ni-Co-Si alloy can promote secondary phase precipitation and refinement, improving activation energy for thermal deformation. Geng et al. (Ref 17, 18) studied the effects of Ti and Ce on rheological stress and activation energy during the thermal deformation of the Cu-Co-Si-Ti alloys. It was discovered that Ti and Ce can impede grain boundary migration and are deleterious to recrystallization nucleation. Yang et al. (Ref 19) demonstrated that trace Y element can raise the hot deformation

---

Qingbao Cao and **Haoyan Hu**, School of Materials Science and Engineering, Henan University of Science and Technology, Luoyang 471023, People's Republic of China; **Meng Zhou, Yi Zhang, Baohong Tian,** and **Yong Liu**, School of Materials Science and Engineering, Henan University of Science and Technology, Luoyang 471023, People's Republic of China; Provincial and Ministerial Co-construction of Collaborative Innovation Center for Non-ferrous Metals New Materials and Advanced Processing Technology, Luoyang 471023 Henan Province, People's Republic of China; and Henan Province Key Laboratory of Nonferrous Materials Science and Processing Technology, Luoyang 471023, People's Republic of China; **Xu Li**, Center for Advanced Measurement Science, National Institute of Metrology, Beijing 100029, People's Republic of China; **Yanlin Jia**, College of Materials Science and Engineering, Central South University, Changsha 410083, People's Republic of China; and **Alex A. Volinsky**, Department of Mechanical Engineering, University of South Florida, 4202 E. Fowler Ave. ENG 030, Tampa 33620. Contact e-mail: zhshgu436@163.com.

activation energy of Cu-Co-Si alloys, as well as promote dynamic recrystallization and refine grains.

To date, there has been limited research regarding the influence of Ce on the flow stress and microstructure evolution in Cu-Fe-Ti-Mg alloys deformed at high temperatures and strain rates. Since the thermal deformation of materials is the foundation of thermal processing, it is commonly utilized to improve the properties of alloys (Ref 20). As a result, the influence of Ce on the hot compression behavior of Cu-Fe-Ti-Mg alloy at high temperatures and high strain rates was explored using a hot compression test in this work. The Gleeble-1500D thermal deformation simulation equipment was used to conduct hot deformation simulation tests. The strain rates were 0.001, 0.01, 0.1, 1, and 10 s^{-1}, and the deformation temperatures were 500, 600, 700, 800, and 950 °C. The stress–strain curves of the Cu-Fe-Ti-Mg and Cu-Fe-Ti-Mg-Ce alloys were obtained, the maximum stress values were measured, and constitutive equations were established. The alloys' microstructure changes as a result of deformation temperature and strain rate are discussed. JSM-7800F field emission transmission electron microscope (TEM) and JEM-2100 high-resolution TEM were used to examine the hot-compressed samples and collect the electron backscatter diffraction (EBSD) data. Analysis was performed regarding the impact of Ce addition on the Cu-Fe-Ti-Mg alloy's microstructure development and thermal activation energy.

2. Experimental Details

The chemical compositions of Cu-Fe-Ti-Mg and Cu-Fe-Ti-Mg-Ce alloys are listed in Table 1. The Cu-Fe-Ti-Mg and Cu-Fe-Ti-Mg-Ce alloys were vacuum smelted from 99% electrolytic copper, pure Fe, Ti, Mg, and Ce in a ZG-0.01 vacuum induction furnace. The temperature was increased to 1200 °C for smelting in a graphite crucible. To keep the crucible dry before smelting, it was heated to 200 °C. The graphite crucible was 180 mm high with an 80 mm inner diameter and 10 kg melting capacity. Argon gas was purged during processing. To prevent alloy spillage during smelting, the largest melting capacity was limited to 8.5 kg. First, pure copper was placed into a vacuum induction furnace and melted, and then other metals were added. The temperature range for the test pour was between 1120 and 1180 °C. Finally, the heated mold was filled with the molten metal and left to cool. The ingot was cleaned from the surface oxide and flash, subsequently homogenized and annealed at 950 °C in a vacuum furnace for 4 h and then cooled with the furnace. The annealed ingot was cut into $\Phi 8 \times 12$ mm cylinders and a small $\Phi 1 \times 2$ mm hole was made in the center of the specimens to fit a thermocouple. After the preparation work was completed, constant strain rate hot compression tests were performed using the Gleeble-1500D hot deformation simulation tester. The strain rate was in the 0.001-10 s^{-1} range, and the deformation temperature was 500-950 °C. This procedure involved heating the samples to the desired temperature at a 20 °C/s rate and held for 6 min to obtain uniform temperature distribution for uniaxial compression. The samples were compressed to 55% strain. The samples were immediately removed and water-cooled after the compression process was completed.

After compression testing, the microstructure of the Cu-Fe-Ti-Mg and Cu-Fe-Ti-Mg-Ce alloys was examined. The samples were sliced perpendicular to the compression axis and etched in 12 mL HCl, 5 g $FeCl_3$, and 85 mL absolute ethanol solution. The metallographic samples were examined using a GX-7A optical microscope. After mechanical and electrolytic polishing, EBSD images were captured using a scanning electron microscope operated at 25 kV. EBSD data were analyzed using Transmission Channel 5 and OIM software. The samples were polished with sandpaper to a 70 μm thickness. They were further thinned with a precision ion polishing system to prepare TEM samples.

3. Results

3.1 Flow Stress Analysis

The true stress–strain curves of the Cu-Fe-Ti-Mg and Cu-Fe-Ti-Mg-Ce alloys deformed under various conditions are shown in Fig. 1. Work hardening and dynamic recrystallization are considered to be the main features of alloy thermal deformation (Ref 12, 21, 22). Stress–strain curve changes can generally be grouped into three types. At the initial stage of plastic deformation, as the strain increases, dislocation density increases, forming entanglements and substructures, leading to strain hardening. In another type, the number of dislocations increases exponentially with strain, but no hardening occurs, and the stress–strain curve flattens due to the annihilation of dislocations and dislocation nodes, and subsequent encounter and cancellation of the dissimilar sign dislocations on the new slip surfaces. The curve first rises to the highest stress value and then plateaus. Dynamic softening occurs in the third type when the flow stress increases with strain due to faster recrystallization. Work hardening is often defined as a rapid increase in the flow stress to a peak value during plastic deformation. The material's strength has now increased significantly, but its flexibility has reduced, and residual internal stresses have been formed within the material. Furthermore, the strain rate and deformation temperature have a substantial impact on the deformation resistance (Ref 23-25). Let us consider the Cu-Fe-Ti-Mg alloy as an example. At a strain rate of 0.01 s^{-1} and a temperature increase from 500 to 950 °C, the alloy's maximum stress reduces from 198.5 to 23.8 MPa. This is because when

Table 1 The nominal and analyzed composition of the alloys

	Analyzed composition, wt.%				
Nominal composition, wt.%	**Fe**	**Ti**	**Mg**	**Ce**	**Cu**
Cu-0.7Fe-0.35Ti-0.08Mg	0.687	0.279	0.061	…	Bal.
Cu-0.7Fe-0.35Ti-0.08Mg-0.15Ce	0.670	0.293	0.056	0.076	Bal.

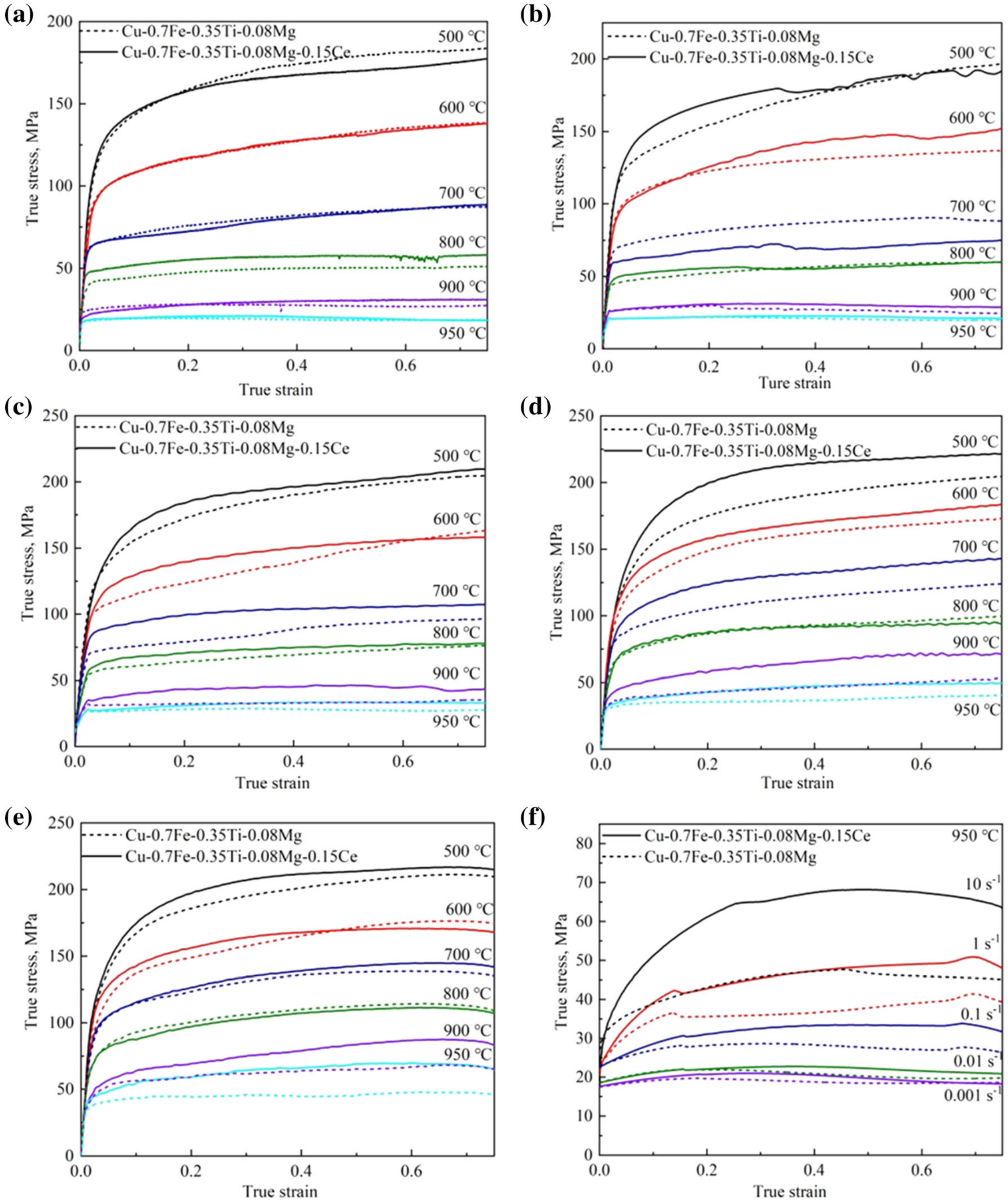

Fig. 1 True stress-true strain curves of the Cu-Fe-Ti-Mg and Cu-Fe-Ti-Mg-Ce alloys deformed at different temperatures and strain rates: (a) 0.001 s^{-1}, (b) 0.01 s^{-1}, (c) 0.1 s^{-1}, (d) 1 s^{-1}, (e) 10 s^{-1}, (f) 950 °C

the temperature rises, the average kinetic energy of the atoms rises as well, lowering the critical stress for the slip of the deformed alloy and allowing for dislocation slip and climb as well as thermal dispersion. As a result, raising the deformation temperature promotes the development of distortion-free equiaxed grains (Ref 26). Furthermore, Ce raises the flow stress of the Cu-Fe-Ti-Mg alloy by 17%. This suggests that Ce slows the recrystallization process (Ref 27).

By comparing the flow stress of the two alloys deformed at 600 °C it was found that the flow stress of the Cu-Fe-Ti-Mg-Ce alloy was significantly higher than the Cu-Fe-Ti-Mg alloy. This is because the addition of Ce can generate oxides, which inhibit dislocation movement and lead to the pinning of grain boundaries, and motivate the precipitation of the secondary phase. Finally, the deformation resistance of the Cu-Fe-Ti-Mg-Ce alloy increases. Geng et al. (Ref 28) also agrees with this point of view.

3.2 Constitutive Equations

The atoms undergo tremendous thermal motion during the plastic deformation of a metal, which requires the atoms to exceed an energy “threshold”, and the needed energy is known as the deformation activation energy. Thermal activation energy is a significant parameter to evaluate the thermal workability of metals. According to the true stress-true strain curves, the hyperbolic sine model was introduced to establish the deformation constitutive equations of the Cu-Fe-Ti-Mg and Cu-Fe-Ti-Mg-Ce alloys.

The Sellars and Mctegart (Ref 29) principal structure equation is a popular tool for predicting and analyzing the relationship between the peak stress σ, deformation temperature T, and the strain rate $\dot{\varepsilon}$ during thermal deformation (Ref 30). The corresponding equations are:

$$\dot{\varepsilon} = A\left[\sinh(\alpha\sigma)^{n}\exp\left(-\frac{Q}{RT}\right)\right] \quad \text{(For all)} \qquad \text{(Eq 1)}$$

$$\dot{\varepsilon} = A_1\sigma^{n_1}\exp\left(-\frac{Q}{RT}\right) \quad (\text{For } \alpha\sigma < 0.8) \qquad \text{(Eq 2)}$$

$$\dot{\varepsilon} = A_2\exp(\beta\sigma)\ \exp\left[-\frac{Q}{RT}\right] \quad (\text{For } \alpha\sigma > 1.2) \qquad \text{(Eq 3)}$$

$$\mathrm{Z} = \dot{\varepsilon}\exp\left[\frac{Q}{RT}\right] = \mathrm{A}[\sinh(\alpha\sigma)]^{n} \qquad \text{(Eq 4)}$$

In the above formulas, R is the universal gas constant (R = 8.31 J mol^{-1} K^{-1}), σ is the peak stress, Q is the deformation activation energy, A, A_1, A_2, n_1, and α are constants, Z is the self-diffusion activation energy of dislocation slip and climb to form the lattice.

It should be pointed out that a steady state is difficult to achieve at high strain rates. As a result, the strain rate at low and high stress levels can be represented using Eq 2 and 3. As indicated in Eq 4, the influence of temperature and strain rate on the flow stress is specified by the Zener–Hollomon parameter (Ref 31-33). Taking the natural logarithms of both sides of Eq 1, 2 and 3 yields:

$$\ln\dot{\varepsilon} = n\ln[\sinh(\alpha\sigma)] - \frac{Q}{RT} + \ln A \qquad \text{(Eq 5)}$$

$$\ln\dot{\varepsilon} = n_1\ln\sigma + \ln A_1 - \frac{Q}{RT} \qquad \text{(Eq 6)}$$

$$\ln\dot{\varepsilon} = \beta\sigma + \ln A_2 - \frac{Q}{RT} \qquad \text{(Eq 7)}$$

In these formulas, n_1 is obtained from the mean of the slopes in Fig. 2(a), and β is the average slope in Fig. 2(b). Taking the Cu-Fe-Ti-Mg-Ce alloy as an example, n_1 = 17.305, β = 0.176, and $\alpha = \beta/n_1$ = 0.01. The partial derivative of Eq 1 can be calculated by keeping the temperature T and the strain rate constant:

$$Q = R\left[\frac{\partial\ln\dot{\varepsilon}}{\partial\ln[\sinh(\alpha\sigma)]}\right]_T\left[\frac{\partial\ln[\sinh(\alpha\sigma)]}{\partial(1/T)}\right] = RnS \qquad \text{(Eq 8)}$$

here n is the strain-hardening exponent, and S is a constant. The mean value of n is obtained from the slopes in Fig. 2(c), and S is obtained from the slopes in Fig. 2(d):n = 11.135, S = 5.217. Q = 482.9 kJ/mol. Taking the natural logarithm of both sides of Eq 4 yields:

$$\ln Z = \ln A + n[\ln(\sinh(\alpha\sigma))] \qquad \text{(Eq 9)}$$

ln A is the intercept in Fig. 2(e), and A = 55.34. The constitutive equation of the Cu-Fe-Ti-Mg-Ce alloy can be expressed as:

$$\dot{\varepsilon} = e^{55.34}[\sinh(0.01\sigma)]^{11.135}\exp\left(-\frac{482,900}{8.314T}\right) \qquad \text{(Eq 10)}$$

Similarly, the thermal activation energy and constitutive equation for the Cu-Fe-Ti-Mg alloy, using $Q = RnS$ = 8.31 × 12.7 × 4.28 = 452 kJ/mol, can be represented as:

$$\dot{\varepsilon} = e^{54.84}[\sinh(0.008\sigma)]^{12.731}\exp\left(-\frac{452,000}{8.314T}\right) \qquad \text{(Eq 11)}$$

It may be concluded that the activation energy of these two materials is greater than pure copper (200 kJ/mol) and Cu-0.4Mg-0.15Ce alloy (255.253 kJ/mol). For pure copper and different alloys, the copper and other alloying element contents are closely associated with strengthening mechanisms such as precipitation and solid solution strengthening. Changes in alloying elements content influence flow stress, which in turn influences the Q value. In addition, the activation energy of the Cu-Fe-Ti-Mg-Ce alloy is 6.8% higher than the Cu-Fe-Ti-Mg alloy. Rare earth elements can encourage the precipitation of compounds, which is the cause of this phenomenon. The threshold stress brought on by precipitates lowers the energy needed for thermal deformation and has higher activation energy (Ref 34).

3.3 Microstructure Evolution

Figure 3 shows the microstructure of the Cu-Fe-Ti-Mg and Cu-Fe-Ti-Mg-Ce alloys deformed under different conditions. Figure 3(a) and (c) illustrates the microstructure of the Cu-Fe-Ti-Mg alloys deformed at the same temperature but at different strain rates. The results show that the grains may be growing at this temperature. By comparing the grain sizes of the two alloys in Fig. 3(a) and (c), it can be seen that the high strain rate shortens the hot deformation time of the alloy, and the recrystallized grains have no time to grow. This suggests that the grains can be successfully refined at a high strain rate. The elongated band spreads from the grain border to the interior of the grain and the grain size increases gradually as a result of the drop in the strain rate and rise in temperature. The microstructure of the Cu-Fe-Ti-Mg-Ce alloy deformed at the same temperature but various strain rates is shown in Fig. 3(b) and (d). Shear bands can be observed in Fig. 3(b), where the grain boundaries become blurred, and the grains elongate along the deformation direction. This means that the presence of strain-gathering regions can lead to stress concentrations and result in work hardening, and consequently, a rapid rise in the flow stress. In their investigation of the hot deformation of Cu-Ni-Si-Cr-Mg alloy, Blaz et al. (Ref 35) discovered that the OLYMPUS PMG3 optical microscope can be used to view the uneven precipitation in the shear zone. The reason for this is that the confined flow increases the coarsening of the precipitates in the shear zone, whereas dynamically coarsened particles cause local matrix softening. In addition, shearing of the material at large strains causes voids to grow and the specimen to fracture. Dynamic recrystallization (Ref 36) is characterized by the steady replacement of distorted grains with fresh equiaxed grains with no distortion, as demonstrated in Fig. 3(d), which shows the creation of fine equiaxed grains without deformation. In places of significant distortion, dynamic recrystallization preferentially

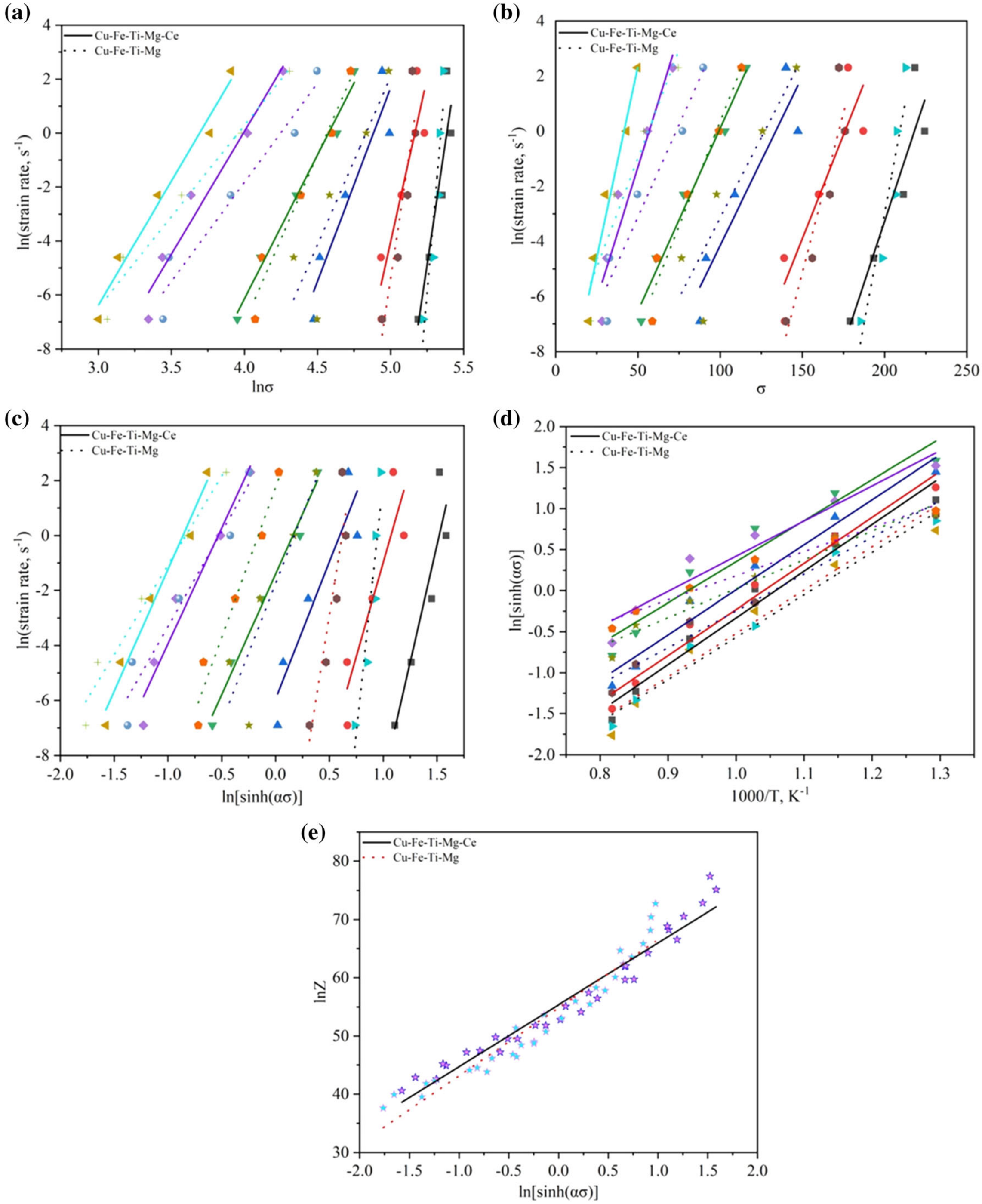

Fig. 2 Relationships between: (a) ln(strain rate) and ln σ; (b) ln(strain rate) and σ; (c) ln(strain rate) and ln[sinh($\alpha\sigma$)]; (d) ln[sinh($\alpha\sigma$)] and 1000/T; (e) lnZ and ln[sinh($\alpha\sigma$)]

creates new distortion-free grain cores and gradually consumes the surrounding deformed matrix. Work-hardening processes are thereby prevented, and stresses are decreased. By comparing the microstructure of the Cu-Fe-Ti-Mg and Cu-Fe-Ti-Mg-Ce alloys deformed at 950 °C and 10 s^{-1} strain rate, it is clear that there are still no distorted grains in the Cu-Fe-Ti-Mg-Ce alloy structure, while the Cu-Fe-Ti-Mg alloy structure has already been completely coarsened. As a consequence, adding Ce significantly delays dynamic recrystallization and refines the grains.

3.4 EBSD Analysis

EBSD was utilized to determine the grain size and shape, as well as crystal orientation (Ref 37, 38). Field emission scanning electron microscopy was used to explore the micro-regional weaving, grain size, and orientation relationships of alloys following hot deformation. Figure 4 depicts EBSD images of the Cu-Fe-Ti-Mg and Cu-Fe-Ti-Mg-Ce alloys deformed under the same conditions. The addition of Ce entirely changed the deformation organization into new, distortion-free fine equiaxed grains and slowed grain growth.

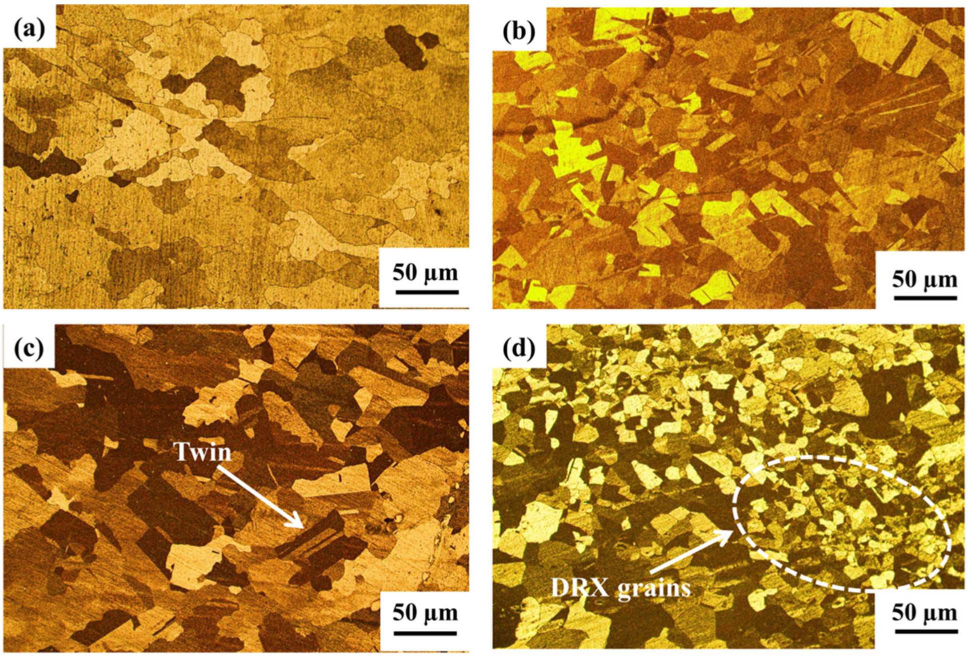

Fig. 3 The microstructure of the Cu-Fe-Ti-Mg and Cu-Fe-Ti-Mg-Ce alloys under different hot deformation conditions: (a) Cu-Fe-Ti-Mg alloy deformed at 950 °C and 0.01 s^{-1}, (b) Cu-Fe-Ti-Mg-Ce alloy deformed at 950 °C and 0.01 s^{-1}, (c) Cu-Fe-Ti-Mg alloy deformed at 950 °C and 10 s^{-1}, (d) Cu-Fe-Ti-Mg-Ce alloy deformed at 950 °C and 10 s^{-1}

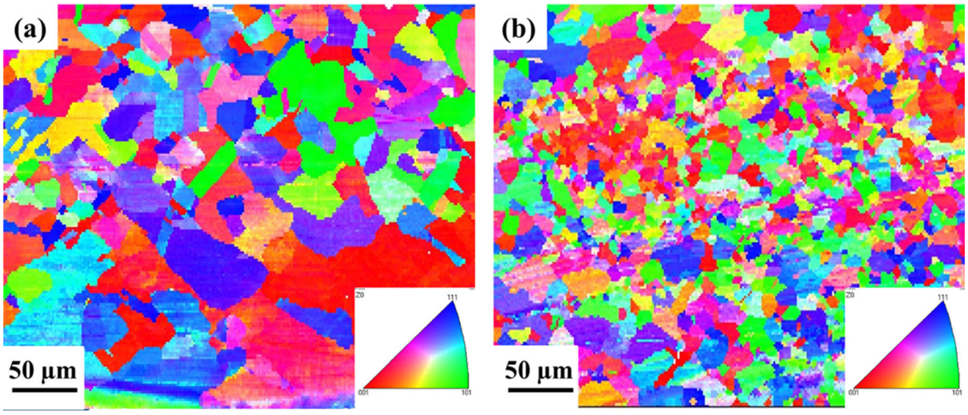

Fig. 4 EBSD diagram of different alloys deformed at 950 °C and 10 s^{-1} strain rate: (a) Cu-Fe-Ti-Mg, (b) Cu-Fe-Ti-Mg-Ce

It is well known that the degree of interfacial migration and deformation is critical in DRX during hot deformation (Ref 39). Furthermore, the sliding and ascent of dislocations are related to the migration of DRX grain borders and grain growth. As a result, the dislocation density near grain boundaries of the Cu-Fe-Ti-Mg and Cu-Fe-Ti-Mg-Ce alloys must be investigated. The geometrically necessary dislocation density is related to local dislocations as in (Ref 40, 41):

$$\rho^{\mathrm{GND}} = \frac{2\theta}{\mu b} \qquad \text{(Eq 12)}$$

here θ is the average local misorientation angle in radians, μ is the scan step size (1 μm, converted to m in calculations), ρ^{GND} is the geometrically necessary dislocation (GND) density in m^{-2}, and b is the 2.55 nm Burger vector, converted to m in calculations. 3° is designated as the critical angle for the average local misorientation value. Since misorientation angles greater than this amount are created by grain boundaries rather than GND accumulation, they are not taken into account in the local dislocation density computations (Ref 17).

Figure 5(a) and (b) shows the dislocation density of the Cu-Fe-Ti-Mg and Cu-Fe-Ti-Mg-Ce alloys deformed at 950 °C and 10 s^{-1} strain rate. The areas with high dislocation density are shown in red, while the low dislocation density areas are marked in blue. It can be found that the GND density of the Cu-Fe-Ti-Mg alloy is 2.7×10^{15} m^{-2}, while the GND of the Cu-Fe-Ti-Mg-Ce alloy is 4×10^{15} m^{-2}. Under high temperature and high strain rate deformation conditions, the Cu-Fe-Ti-Mg alloy with added Ce has a higher dislocation density, implying that the lattice distortion energy inside the crystal is greater, resulting in the material being in a thermodynamically unstable high free energy state, implying that Ce delays the alloy's recrystallization process. This is because the dislocations stored at grain boundaries and crystal defects provide a certain driving force for the nucleation of recrystallized grains, and the result

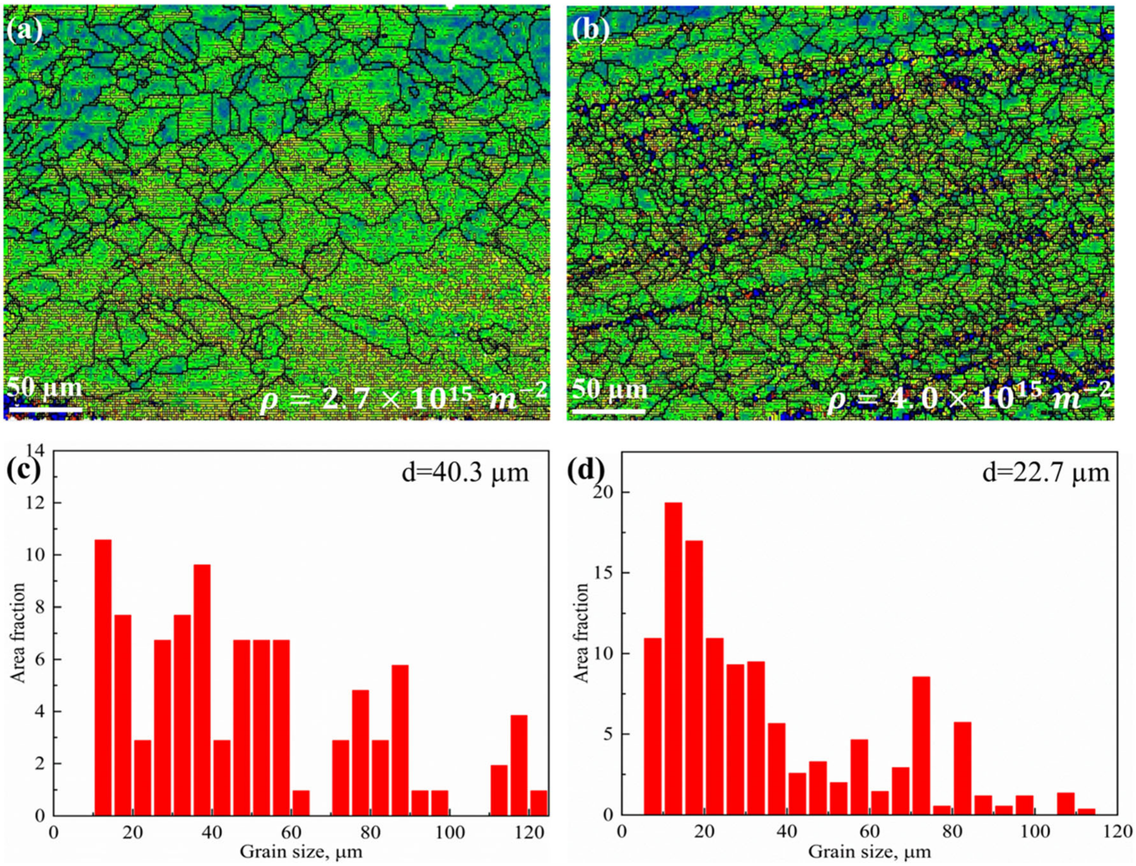

Fig. 5 Kernel average misorientation (KAM) map and grain size distribution of alloys deformed at 950 °C and 10 s^{-1} strain rate: (a), (c) Cu-Fe-Ti-Mg; (b), (d) Cu-Fe-Ti-Mg-Ce (Color figure online)

of recrystallization is to consume dislocations and reduce the dislocation density. This demonstrates that by adding Ce, the Cu-Fe-Ti-Mg-Ce alloy's flow stress and activation energy can be improved, the secondary phase can precipitate more easily, and the grains can be smaller.

Figure 5(c) and (d) shows the grain size distribution of the Cu-Fe-Ti-Mg and Cu-Fe-Ti-Mg-Ce alloys deformed at 950 °C and 10 s^{-1} strain rate. At higher temperatures, dynamic recrystallization is more complete, and distorted grains are gradually replaced by equiaxed grains, which are thus refined. According to Fig. 5(c) and (d), the Cu-Fe-Ti-Mg alloy's average grain size is 40.3 μm, whereas the Cu-Fe-Ti-Mg-Ce alloy's average grain size is 22.7 μm. Under these conditions, the recrystallized grains may tend to grow. The grain size of the Cu-Fe-Ti-Mg-Ce alloy is less than the Cu-Fe-Ti-Mg alloy under the same deformation conditions. It can be observed that Ce inhibits dislocation slip, which is detrimental to the recrystallization nucleation of the Cu-Fe-Ti-Mg-Ce alloy and slows down the recrystallization process.

EBSD grain boundary diagrams of the Cu-Fe-Ti-Mg and Cu-Fe-Ti-Mg-Ce alloys deformed at 950 °C and 10 s^{-1} strain rate are shown in Fig. 6, along with misorientation angle distribution maps. Due to the obvious hampered slip and climb of dislocations in the deformed grain boundaries and process-hardened regions, the misorientation angles are primarily attributed to the low-angle grain boundaries (LAGBs, $< 10°$), with the high-angle grain boundaries (HAGBs) accounting for only a minor portion of the distribution. In Fig. 6(c) and (d), the average misorientation angle increases from 8.7° to 12.7°. This is because there are many regions with poor atomic matching in the grain boundaries of large angles, and there are few bonds between atoms, which is beneficial to the migration of atoms, the recrystallization fraction is increased, and the grains are refined. As has been shown, the HAGBs of the Cu-Fe-Ti-Mg-Ce alloy are lower than the Cu-Fe-Ti-Mg alloy under high temperature and high strain rate deformation conditions. This is due to the higher dislocation density and the greater number of undistorted equiaxed grains in the Cu-Fe-Ti-Mg-Ce alloy compared to the Cu-Fe-Ti-Mg alloy. In other words, the addition of Ce can cause solute atoms to congregate at dislocations and grain boundaries, which hampers grain boundary migration, promotes secondary phase precipitation, and is not favorable to recrystallization nucleation.

To investigate the texture evolution of the Cu-Fe-Ti-Mg and Cu-Fe-Ti-Mg-Ce alloys due to hot deformation, pole figures were obtained. Common face-centered cubic lattice textures in copper alloys include $\{011\}<211>$ Brass texture, $\{011\}<100>$ Gaussian texture, $\{112\}<111>$ copper texture, $\{111\}<211>$ *R* texture, and $\{001\}<100>$ cubic texture (Ref 42, 43). It can be seen from Fig. 7 that the texture of both alloys is the $\{011\}<100>$ Gaussian texture. However, compared with the Pole figures of Fig. 7(a) and (b), the texture strength rose from 4.03 to 6.22. The ODF maps also prove that the addition of Ce improves the texture strength of the Cu-Fe-Ti-Mg alloy. Additionally, it demonstrates that Ce delays the dynamic recrystallization process. The inclusion of Ce can facilitate precipitation in the Cu-Fe-Ti-Mg alloy and refine the grains, as shown by the examination of the true stress–strain

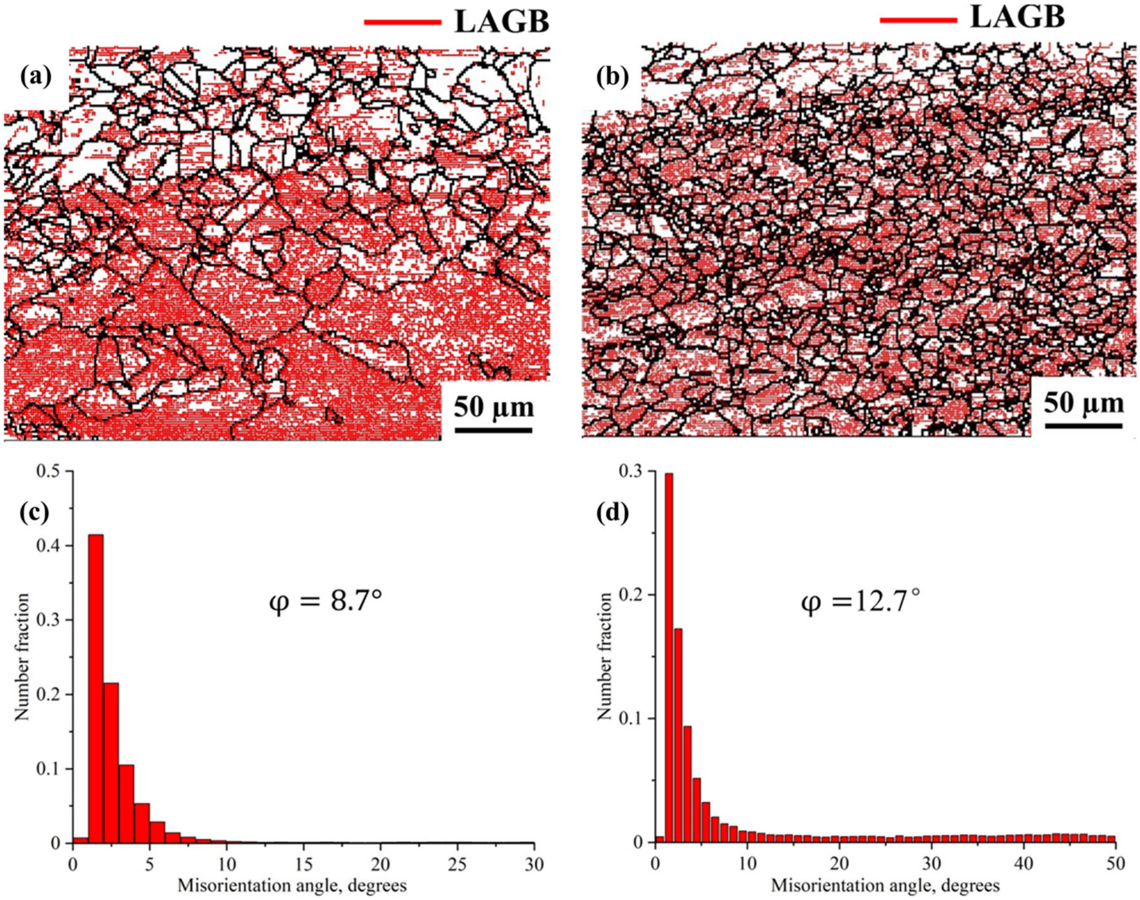

Fig. 6 EBSD grain boundary map and misorientation angle distribution of different alloys deformed at 950 °C and 10 s^{-1} strain rate: (a) and (c) Cu-Fe-Ti-Mg; (b) and (d) Cu-Fe-Ti-Mg-Ce

curve, and microstructure, which is also supported by texture evolution. Yang et al. (Ref 19) proved this.

3.5 TEM Observations

Figure 8 shows TEM images of the Cu-Fe-Ti-Mg-Ce alloy microstructure deformed at 950 °C and 10 s^{-1} strain rate. Figure 8(a) demonstrates that the copper matrix contains a significant number of dislocations and dispersed precipitates. Dislocation movement is often hindered by secondary phases, resulting in the formation of many entangled dislocations and precipitates. Figure 8(b) shows a dislocation cell formed by stacking a large number of dislocations. The dislocations in the cell wall aggregate into a three-dimensional cell-like structure, while the internal dislocation density is relatively low. Dislocation cells often exist in multiple aggregates, which can effectively pin and hinder the migration of dislocations. These typical deformed microstructure characteristics and the pinning of the relative dislocation lines of the precipitation are the intrinsic reasons for the improvement in the stress–strain curves of the alloy. Figure 8(c) is the HRTEM image of Fig. 8(a). The small particle precipitate is spherical, measuring 8.4 nm in length and 9.8 nm in width. According to the superlattice, the Fe_2Ti precipitate is represented as a cubic crystal system, and the lattice constants are $a = b = c = 0.716$ nm. It is confirmed by the inverse fast Fourier transform (FFT) that the precipitated phases lattice constant is coherent with the Fe_2Ti precipitation.

The FFT image in Fig. 8(d) shows that there is an obvious orientation relationship between the Fe_2Ti phase and the copper matrix, which can be expressed as $(2\ \bar{2}0)_{Cu}\|\ (\overline{12}1)_{Fe2Ti}$, $(2\ \bar{2}0)_{Cu}\|(\bar{2}2\bar{2})_{Fe2Ti}$, $(\bar{2}20)_{Cu}\|\ (12\bar{1})_{Fe2Ti}$ and $(\bar{2}20)_{Cu}\|(2\ \bar{2}2)_{Fe2Ti}$. However, $(200)_{Cu}$ and $(\bar{3}0\bar{1})_{Fe2Ti}$, $(\bar{2}20)_{Cu}$ and $(301)_{Fe2Ti}$ are not parallel, and the angles of the diffraction spots have errors of 8.7° and 4.3°, respectively. It is important to note that the angular difference between the $(200)_{Cu}$ and $(\bar{3}0\bar{1})_{Fe2Ti}$ diffraction spots are almost twice the $(\bar{2}20)_{Cu}$ and $(301)_{Fe2Ti}$ diffraction spots. These results indicate that the Fe_2Ti phase maintains a coherent relationship with the Cu matrix. It can be seen from the partially enlarged view of Fig. 8(f) that the Fe_2Ti phase maintains a coherent relationship with the Cu matrix, which will inevitably cause internal stress.

Figure 9 shows the TEM microstructure and selected area electron diffraction pattern (SADP) of the Cu-Fe-Ti-Mg-Ce alloy after deformation at 950 °C and 10 s^{-1} strain rate. Figure 9(a) identifies the analyzed precipitate location. Figure 9(b) is the SADP, which shows a ring shape and the polycrystalline precipitate. It can be found from the energy spectrum in Fig. 9(c) that the precipitate is CuCe. There are many dislocations around the CuCe precipitation phase, so it has high dislocation density, which is a favorable position for the nucleation of the precipitation phase, as well as many fine precipitated Fe_2Ti phase particles distributed around the CuCe.

Thermal deformation creates many dislocations, which encourages the formation of DRX particles and refines the grains. Dislocations can speed up the motion of atoms in metals

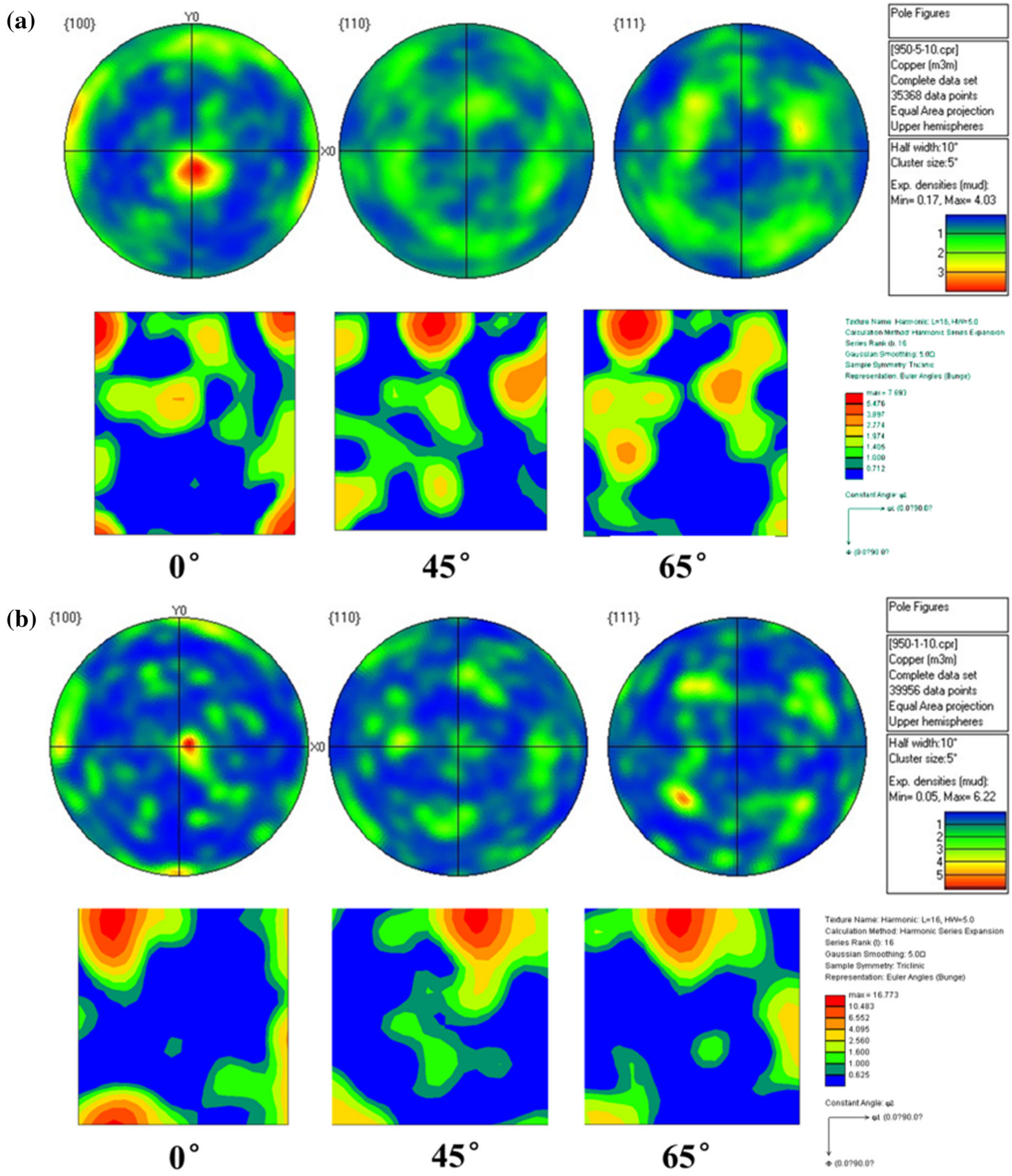

Fig. 7 Pole figures and ODF maps of different alloys deformed at 950 °C and 10 s^{-1} strain rate: (a) Cu-Fe-Ti-Mg; (b) Cu-Fe-Ti-Mg -Ce

and promote the precipitation of alloying elements in the matrix solid solution. However, as the hindering effect of precipitation against dislocations gradually increases, it inhibits the growth of dynamically recrystallized grains, and the dynamically recrystallized grains are refined. Therefore, the continuous dissolution of the Ce alloying element into the matrix promotes the precipitation of Fe_2Ti, and the dislocation movement and recrystallization process are slowed down, which increases the alloy's resistance to deformation.

Many distortion-free equiaxed grains are formed during hot deformation, which promotes grain boundary motion and grain rotation. As a result, a significant number of dislocations proliferate and begin to form dislocation entanglements and cytosolic substructures, improving the alloy's thermal deformation resistance (Ref 44, 45). According to the experimental data, adding Ce to the matrix can improve the deformation resistance and activation energy of the Cu-Fe-Ti-Mg alloy. The microstructure evolution and precipitation phase of the alloy were observed by EBSD and TEM, respectively, and the precipitation mechanism of the alloy was analyzed. EBSD and TEM data analysis shows that the addition of Ce forms some high melting point precipitation phase pegging grain boundaries, which hinders the growth of recrystallized grains and leads to more grain boundaries, thus hindering the movement of

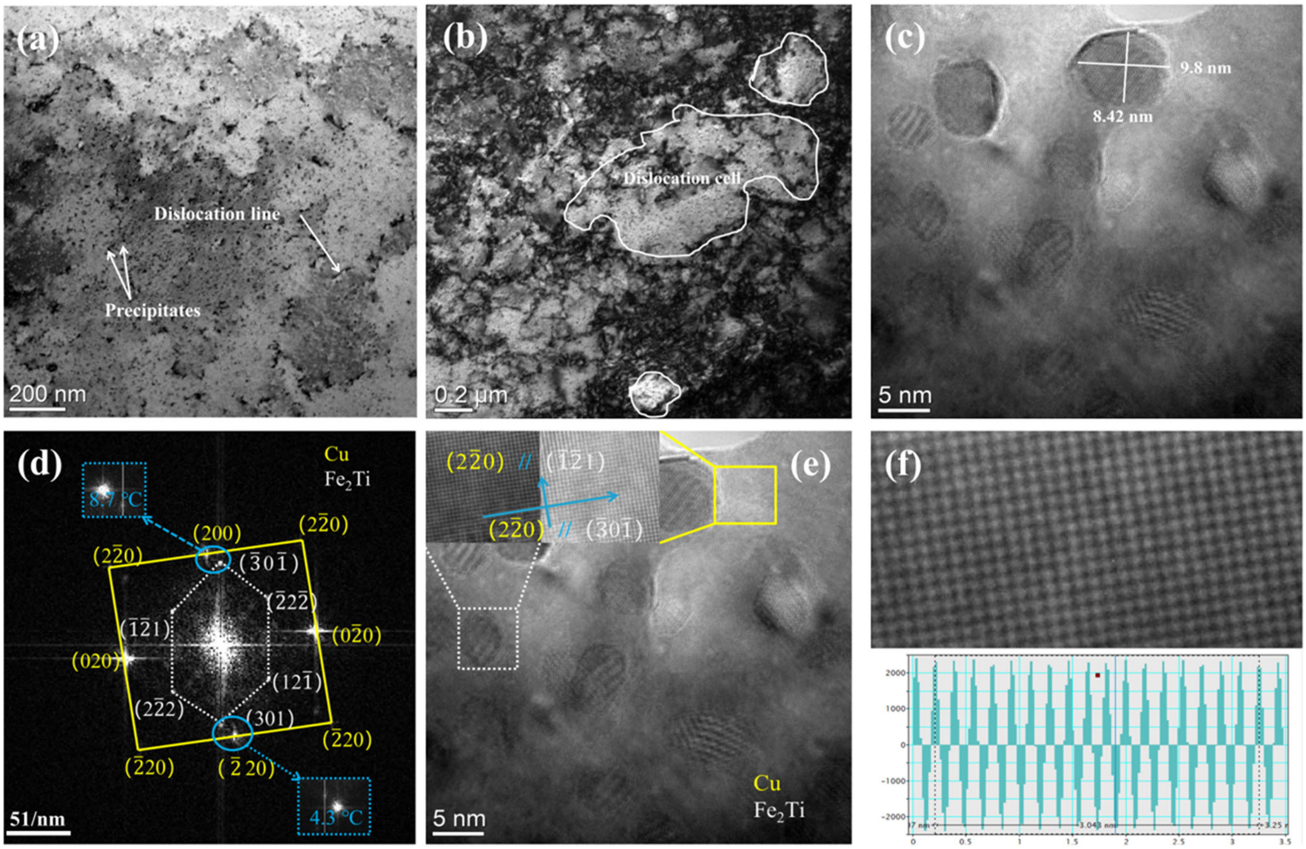

Fig. 8 TEM microstructure of the Cu-Fe-Ti-Mg-Ce alloy after deformation at 950 °C and 10 s^{-1} strain rate: (a) nanoscale precipitates and dislocation lines; (b) dislocation cells; (c) corresponding HRTEM image of precipitation; (d) FFT image of (d); (e) HRTEM image; (f) partial magnification of (e) and measurement of Cu crystals spacing

dislocations and causes a rise in rheological stress, and raises the alloy's activation energy.

4. Discussion

4.1 Effect of Ce on Flow Stress and Activation Energy

Ce decreases the grain size while increasing the alloy's flow stress. The influence of grain refinement is visible in the EBSD microstructure of Cu-Fe-Ti-Mg and Cu-Fe-Ti-Mg-Ce alloys in Fig. 4. Grain refinement and precipitation improve the strength of the alloy. Precipitation increased the activation energy and improved the alloy's high-temperature stability. Furthermore, the addition of Ce makes the structure more uniform during the thermal deformation process. As a result, the Cu-Fe-Ti-Mg-Ce alloy has better high-temperature stability.

4.2 Effect of Ce on the Precipitation Phase

The Cu-Fe-Ti-Mg alloy will result in a series of precipitations after hot compression, in accordance with the experimental results and the analysis of the selected area's diffraction pattern. Similar outcomes were attained during the heat treatment process to the precipitation phase of Cu-Fe-Ti alloy aged at 450 °C studied by Yang (Ref 46). In our experiments, the Fe_2Ti phase forms at 950 °C and 10 s^{-1}. Moreover, the addition of Ce resulted in the formation of more sediment. The presence of precipitates at grain boundaries or dislocations slows their movement and, as a result, increases alloy strength. Furthermore, the alloy structure is refined with the addition of Ce.

4.3 Precipitation Strengthening Mechanism

In this work, the activation energy of the Cu-Fe-Ti-Mg-Ce and Cu-Fe-Ti-Mg alloys under hot compression is 482.9 kJ/mol and 452 kJ/mol, respectively, which is much higher than copper (Ref 47). In this experiment, the n values of the Cu-Fe-Ti-Mg-Ce and Cu-Fe-Ti-Mg alloys are 11.135 and 12.731, respectively, greater than the strain hardening exponent (n = 5 or n = 3) in alloys deformed by dislocation climbing or dislocation sliding mechanisms (Ref 48).

The strength of the alloy can be increased through work hardening, solid solution strengthening, fine crystal strengthening, and precipitation strengthening. The dominant effect of alloy strength is precipitation strengthening, and fine consistent precipitation is more conducive to alloy strengthening. The higher n value shows that the hardening mechanism is by precipitation hardening (Ref 49) and that the precipitates in the matrix impede dislocation migration, resulting in high-strain hardening exponents in these alloys. The primary mechanism of the alloy's plastic deformation is dislocation slip. This viewpoint was also supported by Li et al. (Ref 50, 51). It is worth noting that the addition of Ce increased the activation energy of the alloy Cu-Fe-Ti-Mg by 6.8%. The fundamental reason for this is that the inclusion of Ce causes Fe_2Ti to precipitate more during hot deformation, and more precipitates

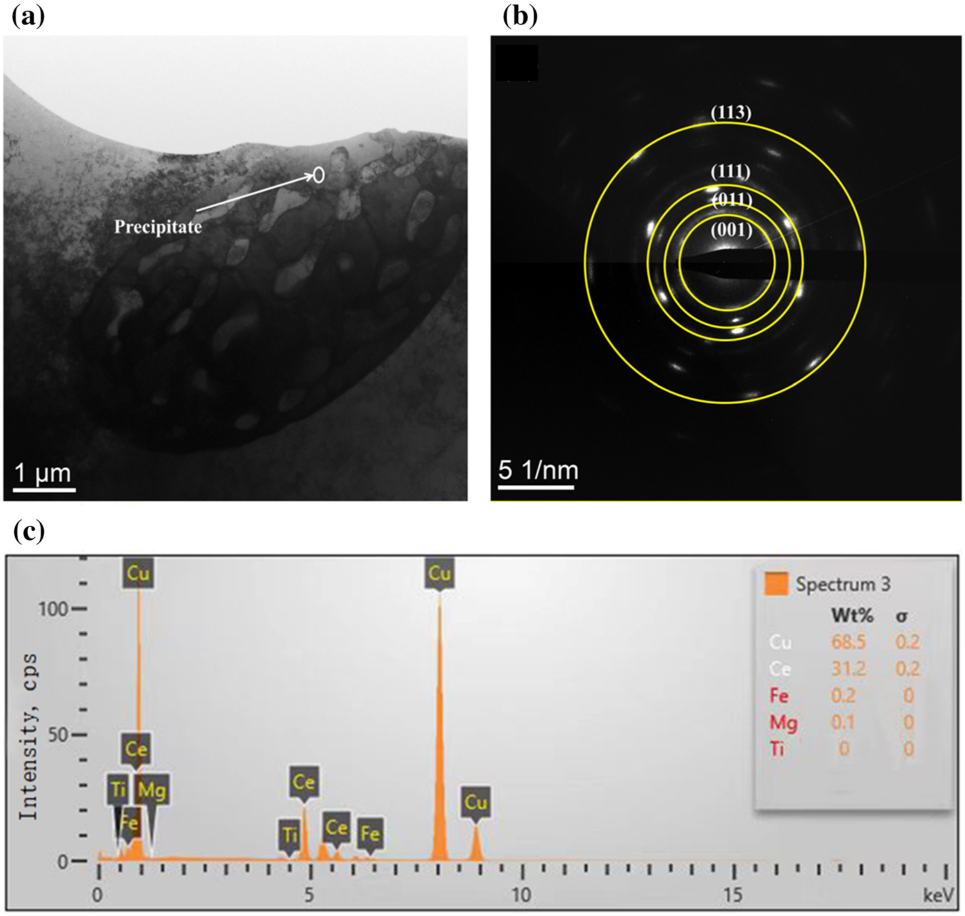

Fig. 9 TEM microstructure of the Cu-Fe-Ti-Mg-Ce alloy after deformation at 950 °C and 10 s^{-1} strain rate: (a) Precipitates; (b) SADP corresponding to precipitation; (c) Energy spectrum corresponding to precipitation

tend to bias on dislocations and grain boundaries, resulting in higher activation energy for hot deformation (Ref 52-54). Another element influencing the alloy's strength is the dynamic precipitation that occurs during hot deformation. Dynamic precipitation significantly increases alloy strength at the high strain rate region (1-10 s^{-1}). The strength and hardness of the material diminish as the strain rate decreases, and the precipitation becomes coarser. Additionally, the alloy is significantly stronger and harder than the precipitation within the grain due to the presence of the precipitation at the grain boundaries. Consequently, the strength and hardness of the alloy are also influenced by the position of the sediment.

5. Conclusions

Thermal processing studies were performed on Cu-Fe-Ti-Mg and Cu-Fe-Ti-Mg-Ce alloys in the 0.001-10 s^{-1} strain rate range at 500-950 °C. The experiments led to the following conclusions.

(1) With an increase in strain rate or a reduction in temperature, the flow stress rises.
(2) The addition of Ce increased the thermal deformation activation energy of the Cu-Fe-Ti-Mg alloy by 6.8%. Linear regression was used to deduce the constitutive equations of the Cu-Fe-Ti-Mg and Cu-Fe-Ti-Mg-Ce alloys.

For the Cu-Fe-Ti-Mg alloy:

$$\dot{\varepsilon} = e^{54.84}[\sinh(0.008\sigma)]^{12.731}\exp\left(-\frac{452,000}{8.314T}\right)$$

For the Cu-Fe-Ti-Mg-Ce alloy:

$$\dot{\varepsilon} = e^{55.34}[\sinh(0.01\sigma)]^{11.135}\exp\left(-\frac{482,900}{8.314T}\right)$$

(3) Under high temperature and high strain rate conditions, the addition of Ce increased the geometrically necessary dislocation density and strength of the Cu-Fe-Ti-Mg alloy, which is not conducive to recrystallization nucleation and nucleation growth, according to EBSD results.
(4) During the hot deformation of the Cu-Fe-Ti-Mg-Ce alloy, many dislocations and Fe_2Ti particles were discovered, and their interaction slowed dislocation movement and improved alloy deformation resistance.

Acknowledgments

This research was supported by the National Natural Science Foundation of China (52071134), the Program for Innovative Research Team at the University of Henan Province (22IRTSTHN001), China Postdoctoral Science Foundation (2020M682316, 2021T140779), and Outstanding Talents Innovation Fund of the Henan Province (ZYQR201912164).

Conflict of interest

The authors declare that they have no known competing financial interests or personal relationships that might influence the work described herein.

References

1. X.H. Zhang, Y. Zhang, B.H. Tian, K.X. Song, P. Liu, Y.L. Jia, X.H. Chen, J.C. An, Z. Zhao, and Y. Liu, Review of Nano-phase Effects in High Strength and Conductivity Copper Alloys, *Nanotechnol. Rev.*, 2019, **8**, p 383–395.
2. H.Y. Yang, K.Q. Li, Y.Q. Bu, J.M. Wu, Y.T. Fang, L. Meng, J.B. Liu, and H.T. Wang, Nanoprecipitates Induced Dislocation Pinning and Multiplication Strategy for Designing High Strength, Plasticity and Conductivity Cu Alloys, *Scripta Mater.*, 2021, **195**, p 113741.
3. Z.L. Zhao, Z. Xiao, Z. Li, W.T. Qiu, H.Y. Jiang, Q. Lei, Z.R. Liu, Y.B. Jiang, and S.J. Zhang, Microstructure and Properties of a Cu-Ni-Si-Co-Cr Alloy with High Strength and High Conductivity, *Mater. Sci. Eng. A*, 2019, **759**, p 396–403.
4. X.H. Zhang, Y. Zhang, B.H. Tian, Y.L. Jia, Y. Liu, and K.X. Song, Cr effects on the Electrical Contact Properties of the Al_2O_3-Cu/15W Composites, *Nanotechnol. Rev.*, 2019, **8**, p 128–135.
5. K.X. Song, Y.F. Geng, Y.J. Ban, Y. Zhang, Z. Li, X.J. Mi, J. Cao, Y.J. Zhou, and X.B. Zhang, Effects of Strain Rates on Dynamic Deformation Behavior of Cu-20Ag Alloy, *J. Mater. Sci. Technol.*, 2021, **79**, p 75–87.
6. I. Batra, G. Dey, U. Kulkarni, and S. Banerjee, Precipitation in a Cu-Cr-Zr Alloy, *Mater. Sci. Eng. A*, 2003, **356**, p 32–36.
7. A. Chbihi, X. Sauvage, and D. Blavette, Atomic Scale Investigation of Cr Precipitation in Copper, *Acta Mater.*, 2012, **60**, p 4575–4585.
8. G. Yang, Z. Li, Y. Yuan, and Q. Lei, Microstructure, Mechanical Properties and Electrical Conductivity of Cu-0.3 Mg-0.05 Ce Alloy Processed by Equal Channel Angular Pressing and Subsequent Annealing, *J. Alloys Compd.*, 2015, **640**, p 347–354.
9. C.D. Xia, Y.L. Jia, W. Zhang, K. Zhang, Q.Y. Dong, G.Y. Xu, and M.P. Wang, Study of Deformation and Aging Behaviors of a Hot Rolled–Quenched Cu-Cr-Zr-Mg-Si Alloy during Thermomechanical Treatments, *Mater. Des.*, 2012, **39**, p 404–409.
10. G.D. Shi, X.H. Chen, H. Jiang, Z.D. Wang, H. Tang, and Y.Q. Fan, Strengthening Mechanisms of Fe Nanoparticles for Single Crystal Cu-Fe Alloy, *Mater. Sci. Eng. A*, 2015, **636**, p 43–47.
11. D.P. Lu, J. Wang, W.J. Zeng, Y. Liu, L. Lu, and B.D. Sun, Study on High-Strength and High-Conductivity Cu-Fe-P Alloys, *Mater. Sci. Eng. A*, 2006, **421**, p 254–259.
12. B.J. Wang, Y. Zhang, B.H. Tian, V. Yakubov, J.C. An, A.A. Volinsky, Y. Liu, K.X. Song, L.H. Li, and M. Fu, Effects of Ce and Y Addition on Microstructure Evolution and Precipitation of Cu-Mg alloy Hot Deformation, *J. Alloy. Compd.*, 2019, **781**, p 118–130.
13. L. Zhang, Z. Li, Q. Lei, W.T. Qiu, and H.T. Luo, Hot Deformation Behavior of Cu-8.0 Ni-1.8 Si–0.15 Mg Alloy, *Mater. Sci. Eng. A*, 2011, **528**, p 1641–1647.
14. H. Zhang, H.G. Zhang, and L.X. Li, Hot Deformation Behavior of Cu-Fe-P Alloys during Compression at Elevated Temperatures, *J. Mater. Process. Technol.*, 2009, **209**, p 2892–2896.
15. C. Zhao, Z. Wang, D.X. Li, D.Q. Pan, B.M. Lou, Z.Q. Luo, and W.W. Zhang, Optimization of Strength and Ductility in an As-Extruded Cu-15Ni-8Sn Alloy by the Additions of Si and Ti, *J. Alloy. Compd.*, 2020, **823**, p 153759.
16. Y.J. Ban, Y. Zhang, Y.L. Jia, B.H. Tian, and X. Li, Effects of Cr Addition on the Constitutive Equation and Precipitated Phases of Copper Alloy during Hot Deformation, *Mater. Des.*, 2020, **191**, p 108613.
17. Y.F. Geng, X. Li, H.L. Zhou, Y. Zhang, Y.L. Jia, B.H. Tian, Y. Liu, A.A. Volinsky, X.H. Zhang, and K.X. Song, Effect of Ti Addition on Microstructure Evolution and Precipitation in Cu-Co-Si Alloy during Hot Deformation, *J. Alloy. Compd.*, 2020, **821**, p 153518.
18. P.H. Geng, G.L. Qin, J. Zhou, T.Y. Li, and N.S. Ma, Characterization of Microstructures and Hot-Compressive Behavior of GH4169 Superalloy by Kinetics Analysis and Simulation, *J. Mater. Process. Technol.*, 2021, **288**, p 116879.
19. P.F. Yang, M. Zhou, Y. Zhang, Y.L. Jia, B.H. Tian, Y. Liu, X. Li, and A.A. Volinsky, Effect of Y Addition on Microstructure Evolution and Precipitation of Cu-Co-Si Alloy during Hot Deformation, *Mater. Charact.*, 2021, **181**, p 111502.
20. K.M. Liu, Z.Y. Jiang, H.T. Zhou, D.P. Lu, A. Atrens, and Y.L. Yang, Effect of Heat Treatment on the Microstructure and Properties of Deformation-Processed Cu-7Cr In Situ Composites, *J. Mater. Eng. Perform.*, 2015, **24**, p 4340–4345.
21. C. Roucoules, M. Pietrzyk, and P. Hodgson, Analysis of Work Hardening and Recrystallization during the Hot Working of Steel Using a Statistically Based Internal Variable Model, *Mater. Sci. Eng. A*, 2003, **339**, p 1–9.
22. Y.Q. Ning, X. Luo, H.Q. Liang, H.Z. Guo, J.L. Zhang, and K. Tan, Competition between Dynamic Recovery and Recrystallization during Hot Deformation for TC18 Titanium Alloy, *Mater. Sci. Eng. A*, 2015, **635**, p 77–85.
23. Z.Y. Ding, S.G. Jia, P.F. Zhao, M. Deng, and K.X. Song, Hot Deformation Behavior of Cu-0.6 Cr-0.03 Zr Alloy during Compression at Elevated Temperatures, *Mater. Sci. Eng. A*, 2013, **570**, p 87–91.
24. G.L. Ji, G. Yang, L. Li, and Q. Li, Modeling Constitutive Relationship of Cu-0.4 Mg Alloy during Hot Deformation, *J. Mater. Eng. Perform.*, 2014, **23**, p 1770–1779.
25. W.L. Cheng, Y. Bai, S.C. Ma, L.F. Wang, H.X. Wang, and H. Yu, Hot Deformation Behavior and Workability Characteristic of a Fine-Grained Mg-8Sn-2Zn-2Al Alloy with Processing Map, *J. Mater. Sci. Technol.*, 2019, **35**, p 1198–1209.
26. N. Tahreen, D.F. Zhang, F.S. Pan, X.Q. Jiang, D.Y. Li, and D.L. Chen, Hot Deformation and Processing Map of an As-Extruded Mg-Zn-Mn-Y Alloy Containing I and W Phases, *Mater. Des.*, 2015, **87**, p 245–255.
27. X. Wang, L.I. Zhou, Z. Xiao, and W.T. Qiu, Microstructure Evolution and Hot Deformation Behavior of Cu-3Ti-0.1Zr Alloy with Ultra-high Strength, *Trans. Nonferrous Met. Soc. China*, 2020, **30**, p 2737–2748.
28. Y.F. Geng, Y. Zhang, K.X. Song, Y.L. Jia, X. Li, H.R. Stock, H.L. Zhou, B.H. Tian, Y. Liu, and A.A. Volinsky, Effect of Ce Addition on Microstructure Evolution and Precipitation in Cu-Co-Si-Ti Alloy during Hot Deformation, *J. Alloy. Compd.*, 2020, **842**, p 155666.
29. X.R. Chen, Q.Y. Liao, Y.X. Niu, W.T. Jia, Q.C. Le, C.L. Cheng, F.X. Yu, and J.Z. Cui, A Constitutive Relation of AZ80 Magnesium Alloy during Hot Deformation Based on Arrhenius and Johnson–Cook Model, *J. Mater. Res. Technol.*, 2019, **8**, p 1859–1869.
30. A. Galiyev, R. Kaibyshev, and G. Gottstein, Correlation of Plastic Deformation and Dynamic Recrystallization in Magnesium Alloy ZK60, *Acta Mater.*, 2001, **49**, p 1199–1207.
31. Y.H. Duan, L.S. Ma, H.R. Qi, R.Y. Li, and P. Li, Developed Constitutive Models, Processing Maps and Microstructural Evolution of Pb-Mg-10Al-0.5 B Alloy, *Mater. Charact.*, 2017, **129**, p 353–366.
32. H. Mirzadeh, J.M. Cabrera, and A. Najafizadeh, Modeling and Prediction of Hot Deformation Flow Curves, *Metall. Mater. Trans. A.*, 2012, **43**, p 108–123.
33. S. Satheesh Kumar, T. Raghu, P.P. Bhattacharjee, G.A. Rao, and U. Borah, Constitutive Modeling for Predicting Peak Stress Characteristics during Hot Deformation of Hot Isostatically Processed Nickel-Base Superalloy, *J. Mater. Sci.*, 2015, **50**, p 6444–6456.
34. Y.F. Geng, Y.J. Ban, B.J. Wang, X. Li, K.X. Song, Y. Zhang, Y.L. Jia, B.H. Tian, Y. Liu, and A.A. Volinsky, A Review of Microstructure and Texture Evolution with Nanoscale Precipitates for Copper Alloys, *J. Mater. Res. Technol.*, 2020, **9**, p 11918–11934.
35. L. Blaz, E. Evangelista, and M. Niewczas, Precipitation Effects during Hot Deformation of a Copper Alloy, *Metall. Mater. Trans. A.*, 1994, **25**, p 257–266.
36. Y. Zhang, H.L. Sun, A.A. Volinsky, B.H. Tian, K.X. Song, B.J. Wang, and Y. Liu, Hot Workability and Constitutive Model of the Cu-Zr-Nd Alloy, *Vacuum*, 2017, **146**, p 35–43.

37. R. Mishnev, I. Shakhova, A. Belyakov, and R. Kaibyshev, Deformation Microstructures, Strengthening Mechanisms, and Electrical Conductivity in a Cu-Cr-Zr alloy, *Mater. Sci. Eng. A*, 2015, **629**, p 29–40.
38. F. Bittner, S. Yin, A. Kauffmann, J. Freudenberger, H. Klauß, G. Korpala, R. Kawalla, W. Schillinger, and L. Schultz, Dynamic Recrystallization and Precipitation Behaviour of High Strength and Highly Conducting Cu-Ag-Zr-Alloys, *Mater. Sci. Eng. A*, 2014, **597**, p 139–147.
39. A.S.H. Kabir, M. Sanjari, J. Su, I.H. Jung, and S. Yue, Effect of Strain-Induced Precipitation on Dynamic Recrystallization in Mg-Al-Sn Alloys, *Mater. Sci. Eng. A*, 2014, **616**, p 252–259.
40. Y.S. Wu, X.Z. Qin, C.S. Wang, and L.Z. Zhou, Influence of Phosphorus on Hot Deformation Microstructure of a Ni-Fe-Cr Based Alloy, *Mater. Sci. Eng. A*, 2019, **768**, p 138454.
41. Y.S. Wu, Z. Liu, X.Z. Qin, C.S. Wang, and L.Z. Zhou, Effect of Initial State on Hot Deformation and Dynamic Recrystallization of Ni-Fe Based Alloy GH984G for Steam Boiler Applications, *J. Alloy. Compd.*, 2019, **795**, p 370–384.
42. C.S. Wang, H.D. Fu, and J.X. Xie, Dynamic Recrystallization Behavior and Microstructure Evolution of High-Performance Cu-3.28Ni-0.6Si-0.22Zn-0.11Cr-0.04P during Hot Compression, *Rare Met.*, 2021, **40**, p 156–167.
43. C. Haase and L.A. Barrales-Mora, Influence of Deformation and Annealing Twinning on the Microstructure and Texture Evolution of Face-Centered Cubic High-Entropy Alloys, *Acta Mater.*, 2018, **150**, p 88–103.
44. M.Y. Li, H. Wang, Y.H. Guo, H.L. Wang, D.D. Zheng, J.F. Shan, and Y.Q. Chang, Microstructures and Mechanical Properties of the nOvel CuCrZrFeTiY Alloy for Fusion Reactor, *J. Nucl. Mater.*, 2020, **532**, p 152063.
45. J. Yi, Y.L. Jia, Y.Y. Zhao, Z. Xiao, K.J. He, Q. Wang, M.P. Wang, and Z. Li, Precipitation Behavior of Cu-3.0Ni-0.72Si Alloy, *Acta Mater.*, 2019, **166**, p 261–270.
46. H.Y. Yang, Y.Q. Bu, J.M. Wu, Y.T. Fang, J.B. Liu, L.Y. Huang, and H.T. Wang, High Strength, High Conductivity and Good Softening Resistance Cu-Fe-Ti Alloy, *J. Alloy. Compd.*, 2022, **925**, p 166595.
47. C. Wang, Y.T. Liu, T. Lin, T.J. Luo, Y.H. Zhao, H. Hou, and Y.S. Yang, Hot Compression Deformation Behavior of Mg-5Zn-3.5Sn-1Mn-0.5Ca-0.5Cu Alloy, *Mater. Charact.*, 2019, **157**, p 109896.
48. D. Jia, W.R. Sun, D.S. Xu, and F. Liu, Dynamic Recrystallization Behavior of GH4169G Alloy during Hot Compressive Deformation, *J. Mater. Sci. Technol.*, 2019, **35**, p 1851–1859.
49. D.Q. Zhou, X.Q. Xu, H.H. Mao, Y.F. Yan, T.G. Nieh, and Z.P. Lu, Plastic Flow Behaviour in an Alumina-Forming Austenitic Stainless Steel at Elevated Temperatures, *Mater. Sci. Eng. A*, 2014, **594**, p 246–252.
50. W.C. Xu, X.Z. Jin, W.D. Xiong, X.Q. Zeng, and D.B. Shan, Study on Hot Deformation Behavior and Workability of Squeeze-Cast 20 vol.% SiCw/6061Al Composites Using Processing Map, *Mater. Charact.*, 2018, **135**, p 154–166.
51. Y. Li and T.G. Langdon, Creep Behavior of an Al-6061 Metal Matrix Composite Reinforced with Alumina Particulates, *Acta Mater.*, 1997, **45**, p 4797–4806.
52. S.J. Zhu, L.M. Peng, Z.Y. Ma, J. Bi, F.G. Wang, and Z.G. Wang, High Temperature Creep Behavior of SiC Whisker-Reinforced Al-Fe-V-Si Composite, *Mater. Sci. Eng. A*, 1996, **215**, p 120–124.
53. A. Sarkar, M. Prasad, and S.N. Murty, Effect of Initial Grain Size on Hot Deformation Behaviour of Cu-Cr-Zr-Ti Alloy, *Mater. Charact.*, 2020, **160**, p 110112.
54. W. Wang, E.Y. Guo, Z.N. Chen, H.J. Kang, Z.J. Chen, C.L. Zou, R.G. Li, G.M. Yin, and T.M. Wang, Correlation between Microstructures and Mechanical Properties of Cryorolled CuNiSi Alloys with Cr and Zr Alloying, *Mater. Charact.*, 2018, **144**, p 532–546.